

Heavy ion anisotropies: a closer look at the angular power spectrum

M. Machado^{1,2}

*Niels Bohr International Academy¹ and Discovery Center²,
Niels Bohr Institute, Blegdamsvej 17, DK-2100 Copenhagen, Denmark*
(Dated: August 23, 2019)

Anisotropies in the final state of heavy-ion collisions carry information on the creation, expansion and evolution of the quark-gluon plasma. Currently, there is an abundance of studies on azimuthal anisotropies in comparison to longitudinal ones. The purpose of this work is to quantify angular (θ, ϕ) correlations to further the understanding of the full spatial 3-D picture of emitted hadrons. Therefore, public ALICE data from Run 1 (2010) of Pb-Pb collisions at $\sqrt{s_{NN}} = 2.76$ TeV is analyzed through the estimation of an angular power spectrum. Issues with $|\eta| < 0.9$ limitation are tackled, as well as event multiplicity and detector efficiency. Firstly, spectra are calculated for toy Monte Carlo samples. Secondly, heavy-ion data spectra are presented for the full momentum phase space $0.15 < p_T < 100$ GeV and also separate intervals $p_T < 0.54$ GeV and $p_T > 0.54$ GeV. The latter reveal how different geometries dominate at distinct scales and transverse momentum. Finally, the study submits particles generated through the AMPT model to the same power spectrum analysis. This comparison shows that in scales dominated by flow geometry, AMPT qualitatively describes the data spectra, while the opposite is true for smaller scales.

I. INTRODUCTION

When two heavy nuclei collide in the Large Hadron Collider (LHC) at ultrarelativistic energies, they form a state of matter denoted quark-gluon plasma (QGP) [1–3] which, as the name indicates, has quarks and gluons as its degrees of freedom. Such is believed to be the state of the universe itself when it was microseconds old. After being formed, the QGP undergoes a collective expansion, i.e., the initial geometry molded by the overlap region and quantum fluctuations dictates the emitted particles final distribution. As the system cools, the quarks and gluons change into hadronic matter through a smooth phase transition. A hadron gas is thus formed and its components finally reach the detectors: these particles carry the only information available on the properties and behavior of this hot primordial soup.

From cosmology, our older window into the early universe comes from the photons emitted from the surface of last scattering, when electrons were bound to nuclei and formed atoms. As the universe expanded, the wavelengths of said photons also stretched. This electromagnetic radiation was first discovered in 1964 by radio astronomers and it is denoted Cosmic Microwave Background (CMB) [4]. The anisotropies present on the latter are an imprint of the initial conditions of our universe. These preferred directions of emission can be studied from the *angular power spectrum* of the CMB, which can determine not only the curvature of the universe, but can be also used to get information on dark-matter and dark-energy densities [5].

Studies on the *azimuthal* anisotropies found in the product of heavy-ion collisions have provided a plethora of insights into QGP formation and evolution: fluctuations in the initial geometry, constraints on shear viscosity to entropy ratio η/s , and the QGP equation of state [6–8]. However, in order to get the full QGP picture, it is necessary to understand its *longitudinal* dynamics.

Still, the latter is yet to be addressed with the same level of scrutiny applied to the transverse evolution. For instance, there is evidence of event-by-event fluctuations in pseudorapidity [9, 10], whose effects distinct models manage to reproduce only qualitatively [11], thus underlying the importance of 3+1D modeling. Additionally, the dependence of η/s on QGP temperature could potentially be probed through longitudinal anisotropies [12], as the temperature profile of the medium changes with pseudorapidity.

An angular power spectrum C_ℓ of heavy ions aims at enriching the understanding of anisotropies in the final particle distribution as a whole: both in the transverse and longitudinal directions. What is more, pseudorapidity η is defined in terms of the polar angle θ between a particle's 3-momentum and the beam axis through $\eta = -\log(\tan(\theta/2))$. This relation enables for converting particles coordinates $(\eta, \phi) \rightarrow (\theta, \phi)$, which allows for power spectrum calculation. Said quantity measures the amplitude of correlations between (θ, ϕ) pairs as a function of angular scale.

This work is a detailed follow-up on the study in Ref. [13]: it also projects heavy-ion ALICE¹ data [14, 15] onto spherical surfaces and calculates their averaged spectrum $\langle C_\ell \rangle$. The first difference lies in the choice of higher map resolution. Additionally, events are separated in accordance to their interaction points, i.e., the position along the beam axis where the collision occurs. The method built in Ref. [13] is then applied for each event batch, considering the usual issues of detector limited acceptance and non-uniform efficiency, as well as relatively low multiplicities. Furthermore, the present study extends the power spectrum estimation for a divided transverse momentum p_T phase space: $p_T < 0.54$ GeV and $p_T > 0.54$ GeV. Finally, spectra results are compared to

¹ A Large Ion Collider Experiment

a multi-phase transport (AMPT) model [16] for a single centrality class, 10-20%. A difference in scales is clearly observed, with the model succeeding in one, though failing the other.

The first part of this paper details the method built in Ref. [13] for toy Monte Carlo simulations under the new chosen resolution. The MC distributions are sampled from functions of the type $f_{MC}(\theta, \phi) = g(\theta)h(\phi)$. On the second part, the angular power spectrum of Pb-Pb collisions at 2.76 TeV center-of-mass energy is presented for the ALICE Run 1 2010 data set from the CERN open data portal [14]. The results are displayed for the full and partial p_T intervals in the following centralities: 0-5%, 5-10%, 10-20%, 20-30%, and 30-40%.

II. BUILDING A METHOD

Particles emitted from nuclei collisions have their coordinates represented in terms of pseudorapidity η , azimuthal angle ϕ and transverse momentum p_T . As previously mentioned, the data set at hand was recorded with the ALICE detector [17, 18] in 2010, during Run 1 of LHC at a center-of-mass energy per nucleon of $\sqrt{s_{NN}} = 2.76$ TeV [14].

The extraction of said ALICE data along with its event selection and default cuts were executed through the repository in Ref. [15]. The algorithm begins by verifying whether a primary vertex z_{vtx} exists, i.e., if the particles came from a heavy-ion collision or from vacuum chamber interactions. The next step then consists in checking if z_{vtx} lies within 10 cm of the detector's center. In addition, event multiplicity should be non-zero. Lastly, a minimum-bias trigger selects high efficiency events [18].

The tasks of primary and secondary vertex determination, as well as track reconstruction, centrality estimation and separation of particle beam from background are performed by the following subsystems: the Inner Tracking System (ITS) [19], the Time Projection Chamber (TPC) [20] and the VZERO (V0) detectors [21]. Through the combination of their capabilities and event selection criteria, the phase space coverage at present is $|\eta| < 0.9$, $0.15 < p_T < 100$ GeV and $0 \leq \phi < 2\pi$.

The main objective of this work lies in mapping the heavy-ion events onto tessellated spheres. As a first step, the final particle distribution $f(\eta, \phi, p_T)$ should undergo a change of variables from pseudorapidity to polar angle through the expression $\theta = 2 \arctan(e^{-\eta})$; explicitly, $f(\eta, \phi, p_T) \rightarrow f(\theta, \phi, p_T)$. The software package HEALPix² [22] (Hierarchical Equal Area isoLatitude Pixelation) was employed for both map projections and power spectrum calculations. As the name itself suggests, it divides the surface of a sphere into pixels of equal areas.

The number of pixels N_{pix} is directly related to the resolution parameter N_{side} through $N_{pix} = 12N_{side}^2$. In

the previous study [13] the chosen resolution was $N_{side} = 8$. However, due to concerns over signal smoothing of events from most central collisions, the present resolution is $N_{side} = 16$.

During the course of this paper event maps are made by counting the particles with coordinates (θ, ϕ) that fall within each pixel boundaries. More specifically, heavy-ion data or samples of a function $f(\theta, \phi)$ are sets of unit vectors $\hat{\mathbf{n}} = (\theta, \phi)$. Each of their entries (θ_j, ϕ_j) correspond to a pixel on a map: the 2-D angular distribution turns into an 1-D array of pixels indexed $p \in [0, N_{pix})$ from $\theta = 0$ to $\theta = \pi$. Lastly, it should be remarked that p_T will not be considered in this first part of the discussion.

Let $\mathbf{n}_p = (\theta_p, \phi_p)$ be the pixel center coordinates, then $f(\mathbf{n}_p)$ represents the pixelated map of $f(\hat{\mathbf{n}})$. For a distribution on the surface of a tessellated sphere, the $a_{\ell m}$ coefficients of the spherical harmonic expansion can be estimated as

$$a_{\ell m} = \sum_{p=0}^{N_{pix}-1} \Omega_p f(\mathbf{n}_p) Y_{\ell m}^*(\mathbf{n}_p), \quad (1)$$

where $\Omega_p = 4\pi/N_{pix}$ is the standard pixel weight under HEALPix.

The angular power spectrum C_ℓ is defined as the variance, or second moment, of the $a_{\ell m}$ for a given ℓ . The later are denoted *multipole*, with $\ell = 0$ being the monopole, $\ell = 1$ the dipole and so on. The expression for C_ℓ is

$$\langle a_{\ell m} a_{\ell' m'}^* \rangle = \delta_{\ell\ell'} \delta_{mm'} C_\ell, \quad C_\ell = \frac{1}{2\ell+1} \sum_{m=-\ell}^{\ell} |a_{\ell m}|^2. \quad (2)$$

Following up, we discuss in detail the effects on the spectrum under limited detector coverage, how to estimate the background caused by low multiplicity and non-uniform detector efficiency for a MC generated distribution.

A. The mask effect

The acceptance of a detector may be represented by the function $W(\hat{\mathbf{n}})$, also denoted as *mask*. The true underlying distribution $f_{tru}(\hat{\mathbf{n}})$ then relates to the observed one $f_{obs}(\hat{\mathbf{n}})$ through $f_{obs}(\hat{\mathbf{n}}) = W(\hat{\mathbf{n}}) f_{tru}(\hat{\mathbf{n}})$. Also, for a perfect detector $W(\hat{\mathbf{n}}) = 1, \forall \hat{\mathbf{n}}$.

Under $W(\hat{\mathbf{n}})$ the $a_{\ell m}$ coefficients of the maps in question, i.e., the ones accessible experimentally, become a linear combination of the coefficients pertaining to the true distributions under full detector coverage $\tilde{a}_{\ell m}$. For the current data set, $W(\hat{\mathbf{n}}) = 1$ if $44^\circ \lesssim \theta \lesssim 136^\circ$ and zero otherwise. In addition, the azimuthal direction is

² <https://healpix.sourceforge.io/>

completely covered. The harmonic coefficients are related as follows:

$$a_{\ell m} = \sum_{\ell'} \sum_{m'=-\ell'}^{\ell'} \underbrace{\left[\int_{\Omega_\eta} Y_{\ell'm'}(\hat{\mathbf{n}}) Y_{\ell m}^*(\hat{\mathbf{n}}) d\Omega \right]}_{W_{mm'}^{\ell\ell'}} \tilde{a}_{\ell'm'}, \quad (3)$$

where Ω_η is the region covered by the detector.

The mixing matrix $W_{mm'}^{\ell\ell'}$ associated with the mask $W(\hat{\mathbf{n}})$ is depicted in Fig. 1 for a maximum multipole value $\ell_{max} = 47$ corresponding to the chosen resolution. Each one of the major squares refers to a fixed combination of $m, m' = 0, 1$ with varying ℓ, ℓ' . The gray areas indicate $m \neq m'$, which yield null values for the matrix, since detector coverage encompasses the full azimuth. Another noteworthy feature of $W_{mm'}^{\ell\ell'}$ is the chessboard-like pattern of $m = m'$: it means that ℓ, ℓ' must have the same parity. Additionally, the matrix values decrease with increasing $\Delta\ell = |\ell' - \ell|$, so only harmonics with neighboring multipole values contribute to the observed $a_{\ell m}$.

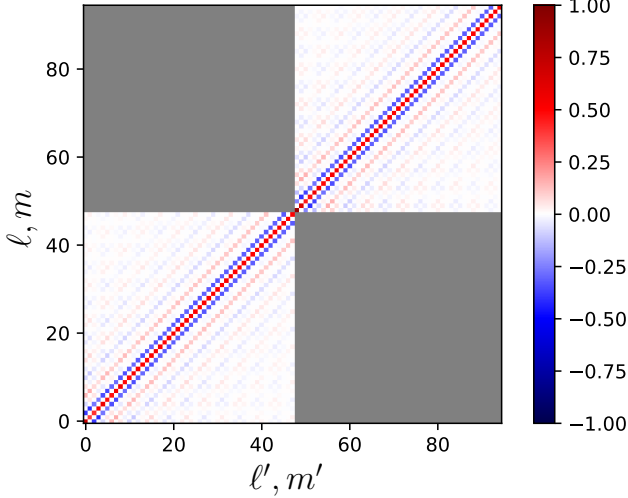


FIG. 1. Mixing matrix $W_{mm'}^{\ell\ell'}$ for $m, m' = 0, 1$ and truncated to $\ell_{max} = 47$.

The linear system in Eq. (3) has no unique solution, due to $W_{mm'}^{\ell\ell'}$ having a determinant equal to zero. In this case, it is not possible to get the true $\tilde{a}_{\ell m}$ values by inverting the matrix. The solution proposed in Ref. [13] relies on the fact that $a_{\ell 0}$ coefficients with ℓ even are the ones mostly affected by the mask geometry. The aforementioned work shows how fully isotropic distributions have a particular enhancement of even modes relative to odd ones solely due to $W(\hat{\mathbf{n}})$. It is straightforward to verify with Eq. (3) that \tilde{a}_{00} alongside $W_{mm'}^{\ell\ell'}$ make it so that only $a_{\ell 0}$ with ℓ even are non-zero. Accordingly, all remaining modes should be zero, which provides an interesting asset to the method at hand.

From Ref. [13], anisotropies are best accounted for when $m = 0$ modes are eliminated from C_ℓ . The following expression for the power spectrum is hence used throughout the analysis:

$$C_\ell^{m \neq 0} = \frac{1}{2\ell + 1} \sum_{m=-\ell}^{\ell} |a_{\ell m}|^2 - \frac{|a_{\ell 0}|^2}{2\ell + 1}. \quad (4)$$

B. The multiplicity issue

The averaged angular power spectrum $C_\ell^{m \neq 0}$ of isotropic maps limited to $|\eta| < 0.9$ should be equal to zero for all ℓ . Nevertheless, for generated isotropic distributions with multiplicity akin to those of the 0-5% centrality, their averaged spectrum $\langle C_\ell^{m \neq 0} \rangle_{iso}$ is of order $\mathcal{O}(10^{-3})$ [13]. This suggests that each ℓ -mode of the spectra carries a quantity attributed to the distributions' multiplicity M .

In order to quantify how the observed spectrum values change with typical event multiplicity, a simple approach was devised: we generated a set of 8000 isotropic events where they all have the same multiplicity and calculated $\langle C_\ell^{m \neq 0} \rangle_{iso}$. This process is repeated from $M = 100$ to $M = 5000$. Additionally, the value of $\langle C_\ell^{m \neq 0} \rangle_{iso}$ for each ℓ is plotted as a function of the multiplicity set and fitted to a power law of the type $p_0 \cdot M^{-p_1} + p_2$, where p_i for $i = 0, 1, 2$ are the fit parameters.

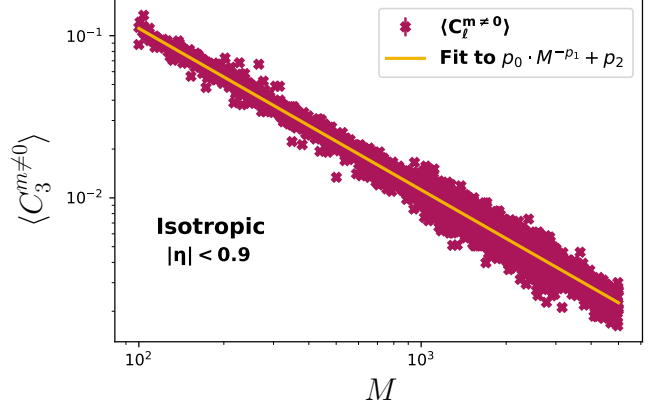


FIG. 2. $\langle C_3^{m \neq 0} \rangle_{iso}$ as a function of multiplicity (M).

Notice in Fig. 2 how $\langle C_3^{m \neq 0} \rangle_{iso}$ decreases with higher multiplicity according to a power law, a feature that is true to all modes. It is worth noticing that p_2 should be the 'true' $\langle C_\ell^{m \neq 0} \rangle$ value when multiplicity tends to infinity. One could be tempted in this case to correct the spectrum values by finding p_0, p_1 and subtracting $\langle p_0 \cdot M^{-p_1} \rangle$ from the observed $\langle C_\ell^{m \neq 0} \rangle$. However, the relation in Fig. 2 could be dependent on the underlying distribution. Instead, we make use of the non-zero result of $\langle C_\ell^{m \neq 0} \rangle_{iso}$ itself for a given multiplicity distribution.

Let $\langle N_\ell^{m \neq 0} \rangle$ be the averaged background spectrum associated with the typical event multiplicity. We begin by producing $\sim 10^6$ isotropic events according to the present multiplicity distribution within $|\eta| < 0.9$ and calculating their power spectra. At the end, the ensemble average is taken thus yielding $\langle N_\ell^{m \neq 0} \rangle$. This power spectrum should give an estimate on the sparsity background, i.e. the size of fluctuations originated solely from typical event multiplicity.

A simple approach to correcting the averaged power spectrum of a given set of events would be to subtract from it the corresponding $\langle N_\ell^{m \neq 0} \rangle$ to its multiplicity. This can be thought as akin to comparing the signal-to-background ratio to unity $|\langle C_\ell^{m \neq 0} \rangle / \langle N_\ell^{m \neq 0} \rangle - 1|$. Since the only difference is a normalization factor, we define $\langle S_\ell^{m \neq 0} \rangle = |\langle C_\ell^{m \neq 0} \rangle - \langle N_\ell^{m \neq 0} \rangle|$ the averaged angular power spectrum corrected by the low event multiplicity.

In order to test the efficacy of this correction, two sets of Monte Carlo distributions are generated. Their underlying functions have the form $f_{MC_1}(\hat{\mathbf{n}}) = h(\phi)$ and $f_{MC_2}(\hat{\mathbf{n}}) = g(\theta)h(\phi)$, with

$$g(\theta) \propto \cosh\left(\frac{\theta - \pi/2}{2}\right) ((\theta - \pi/2)^2 + 1),$$

$$h(\phi) \propto \left[1 + 2 \sum_{n=1}^6 v_n \cos(n(\phi - \Psi_n))\right], \quad (5)$$

where v_n are fixed coefficients of the Fourier expansion (shown in Table I) and Ψ_n varies randomly event-by-event for each n . The same number of events $N_{evts} \sim 8000$ were generated for both mentioned functions, with same multiplicity distributions. These simulated events were then projected onto maps and had their power spectra calculated. Finally, the average was taken resulting in $\langle C_\ell^{m \neq 0} \rangle_{MC_1}$ and $\langle C_\ell^{m \neq 0} \rangle_{MC_2}$. The same background spectrum $\langle N_\ell^{m \neq 0} \rangle$ was used for both their corrections, $\langle S_\ell^{m \neq 0} \rangle_{MC_1}$ and $\langle S_\ell^{m \neq 0} \rangle_{MC_2}$.

v_1	v_2	v_3
0.02119	0.05928	0.02636
v_4	v_5	v_6
0.01218	0.00520	0.00209

TABLE I. Values of v_n coefficients for $h(\phi)$.

The resulting spectra $\langle S_\ell^{m \neq 0} \rangle_{MC_1}$ and $\langle S_\ell^{m \neq 0} \rangle_{MC_2}$ are compared to the analytically calculated ones $C_\ell^{m \neq 0}$ directly from $f_{MC_1}(\hat{\mathbf{n}})$ and $f_{MC_2}(\hat{\mathbf{n}})$. These are depicted in Fig. 3 until $\ell = 20$. Notice how they fit the direct calculation quite closely for $1 \leq \ell \leq 6$. At higher ℓ modes the influence of the v_n coefficients decreases with smaller scales. It is an unsurprising outcome, since the geometry generated by initial condition fluctuations belongs to large scales, or low ℓ .

At this point one can notice from Fig. 3 how the angular power spectrum of distributions purely dominated by

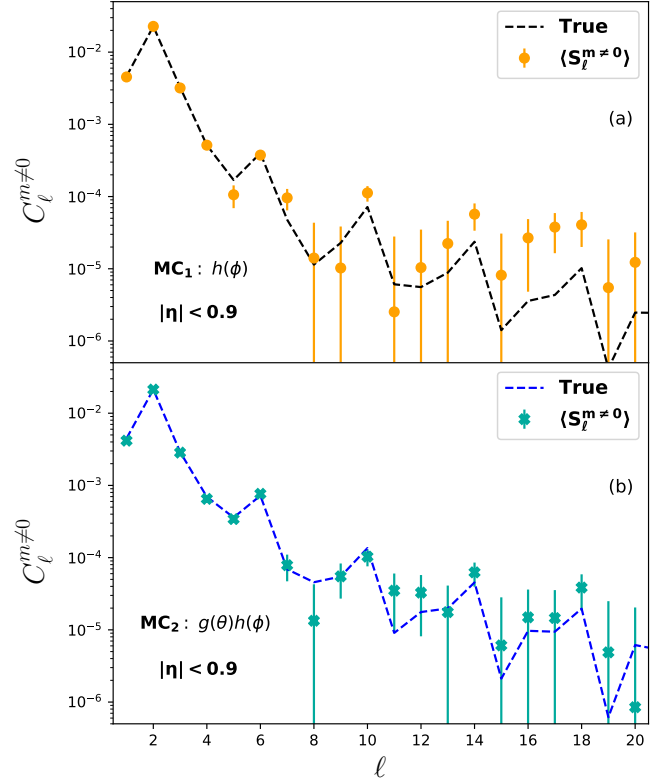


FIG. 3. Comparison between corrected $\langle S_\ell^{m \neq 0} \rangle$ and the analytically calculated spectra for both MC functions.

flow should look like. The peak in $\ell = 2$ pertains to the almond-like shape of the overlapping nuclei. It also influences $\ell = 6$, since v_2 also contributes to C_6 . Though their values differ, the shapes of $\langle S_\ell^{m \neq 0} \rangle_{MC_1}$ and $\langle S_\ell^{m \neq 0} \rangle_{MC_2}$ are basically the same, specially at the low ℓ region.

Overall, the method of correction described above managed to perform remarkably well for $\ell \leq 6$, while becoming trickier for higher values. The limitations of the correction are probably dependent on the distributions at hand, since it is clear to see that MC_2 was better estimated than MC_1 on the $7 \leq \ell \leq 10$ region. Before moving on to heavy-ion data, it is necessary to ascertain that the strategy applied in Ref. [13] to deal with detector efficiency actually works.

C. Detector efficiency

The collisions of heavy ions have different azimuthal orientations relative to each other, implying that if they were to be summed over, the result would be isotropic in ϕ . Namely, $\sum_{i=0}^{N_{evts}-1} f^{(i)}(\mathbf{n}_p) \propto g(\mathbf{n}_p)$, with $f^{(i)}(\mathbf{n}_p)$ as the map of a single event i and $g(\mathbf{n}_p)$ representing the pixelation of $g(\theta)$. Such overlapping of collisions is shown in Fig. 4 for the 10-15% centrality. However, anisotropies are clearly seen, which suggests they are caused by the detector's efficiency. In the following calculations, we

consider the MC_2 distribution, since it possesses $g(\theta)$, making it closer to the data itself.

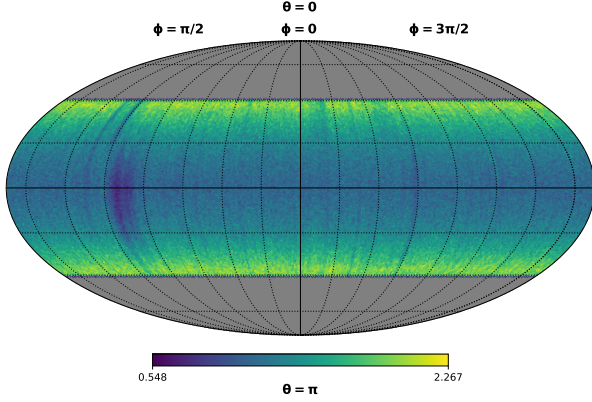


FIG. 4. Overlapping map $F^{all}(\mathbf{n}_p)$ of ~ 8000 events belonging to the 10-15% centrality.

Assuming the detector's efficiency to be a function of the polar and azimuthal angles, $D(\hat{\mathbf{n}})$, with corresponding map $D(\mathbf{n}_p)$. Since each event is subjected to the same detector performance, then their particle distribution on the sphere $f_{MC_2}^{(i)}(\mathbf{n}_p)$ should instead be $f_{D_2}^{(i)}(\mathbf{n}_p) = D(\mathbf{n}_p) \cdot f_{MC_2}^{(i)}(\mathbf{n}_p)$, where $f_{D_2}^{(i)}(\mathbf{n}_p)$ designates the observed event particle distribution map under detector effects. In light of these new considerations, the overlapping distribution of the observed events will be

$$\begin{aligned} F^{all}(\mathbf{n}_p) &= \sum_{i=0}^{N_{events}-1} f_{D_2}^{(i)}(\mathbf{n}_p) \\ &= D(\mathbf{n}_p)g(\mathbf{n}_p). \end{aligned} \quad (6)$$

In order to verify the changes in spectrum values associated with the detector anisotropies, a 2-D spline of $D(\mathbf{n}_p)$ was created to estimate $D(\hat{\mathbf{n}})$. Then, ~ 8000 events with underlying function $D(\hat{\mathbf{n}})f_{MC_2}(\hat{\mathbf{n}})$ were generated, had their spectra calculated and averaged over. The same background spectrum $\langle N_\ell^{m \neq 0} \rangle$ applied to MC_1 and MC_2 above was used to compute $\langle S_\ell^{m \neq 0} \rangle_{D_2}$. On the follow-up, both corrected spectra $\langle S_\ell^{m \neq 0} \rangle_{MC_2}$ and $\langle S_\ell^{m \neq 0} \rangle_{D_2}$ are divided by the analytically calculated $C_\ell^{m \neq 0}$ for MC_2 . These ratios are shown in Fig. 5.

Notice in Fig. 5 how, in the region $\ell \leq 6$ where the coefficients v_n have most influence, it is possible to see a deviation at $\ell = 4, 5, 6$. Interestingly, $\ell = 8$ is the most accentuated mode when checking the ratio $\langle S_\ell^{m \neq 0} \rangle_{D_2} / C_\ell^{m \neq 0}$. After all, it corresponds precisely to the scale $\sim 22.5^\circ$ of the dark patch in Fig. 4.

In the previous work [13], the trick employed to deal with detector-caused anisotropies was dividing each event by $F^{all}(\mathbf{n}_p)$. The same approach is used here:

$$\bar{f}_{D_2}(\mathbf{n}_p) = \frac{f_{D_2}(\mathbf{n}_p)}{D(\mathbf{n}_p)g(\mathbf{n}_p)}. \quad (7)$$

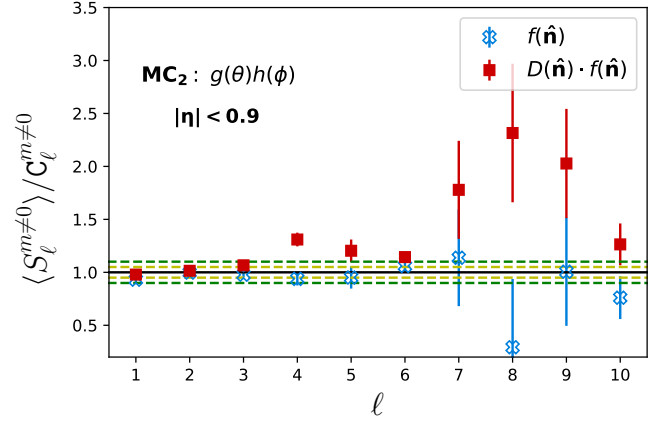


FIG. 5. Ratios $\langle S_\ell^{m \neq 0} \rangle / C_\ell^{m \neq 0}$ for MC_2 under detector with uniform and non-uniform efficiencies. Dashed lines are 1σ (yellow) and 2σ (green) deviations for $f_{MC_2}(\hat{\mathbf{n}})$ within $1 \leq \ell \leq 6$ from unity.

Note how the latter results are also divided by their multiplicity density distribution in θ . Therefore, besides the changes on $\langle C_l \rangle$ due to smoothing out the detector anisotropies, there should be the additional effect of changing the overall θ distribution. In other words, the pixels in $\bar{f}_{D_2}(\mathbf{n}_p)$ will have associated weights coming from both detector efficiencies and the distribution along the polar angle. Nevertheless, the pixel density will remain unchanged, as the ones with null value shall stay like that.

A direct consequence of dividing by $g(\mathbf{n}_p)$ lies in the estimation of $\langle N_\ell^{m \neq 0} \rangle$. A new calculation was thus devised: we take an event, randomize its azimuthal distribution to get rid of the ϕ dependency and then divide it by the average event map, $g(\mathbf{n}_p)$. This process is repeated $\sim 10^6$ times, each turn taking a random event. Finally the averaged power spectrum is calculated, here denoted $\langle N_\ell^{m \neq 0} \rangle_{bar}$. These normalized azimuthally isotropic events possess the same trait as $\bar{f}_{D_2}(\mathbf{n}_p)$, namely weighted pixels whose densities follow $g(\mathbf{n}_p)$.

It should also be remarked that Eq. (7) implies that $\bar{f}_{D_2}(\mathbf{n}_p)$ will have a spectrum like $f_{MC_1}(\hat{\mathbf{n}})$, since its polar distribution has been smoothed out. We denote the corrected power spectrum of $\bar{f}_{D_2}(\mathbf{n}_p)$ as $\langle S_\ell^{m \neq 0} \rangle_{bar}$ and compare it to $C_\ell^{m \neq 0}$ pertaining to $f_{MC_1}(\hat{\mathbf{n}})$. The result can be seen in Fig. 6 (a), where the modes enhanced by the detector anisotropies have been successfully suppressed.

From Fig. 6 (b), the ratios for $\ell \leq 6$ stand within 1σ deviation. On the other hand, the error on the estimation of the higher modes is significantly wide, though still comparable to MC_1 itself. It has been mentioned that in this region the influence of v_n wanes, making way for the detector anisotropies. So it is not surprising that this region has wide error bars.

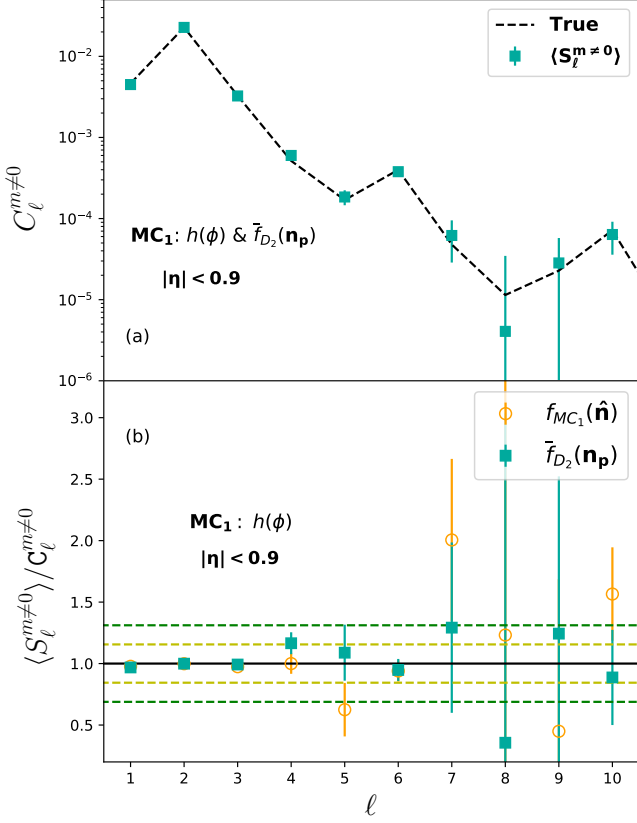


FIG. 6. Efficiency-corrected spectrum $\langle S_\ell^{m \neq 0} \rangle_{bar}$ in comparison to the expected MC_1 spectrum (a). Ratios $\langle S_\ell^{m \neq 0} \rangle / C_\ell^{m \neq 0}$ for $f_{MC_1}(\hat{\mathbf{n}})$ and $\bar{f}_{D_2}(\mathbf{n}_p)$ (b). Dashed lines are 1σ (yellow) and 2σ (green) deviations of the MC_1 ratio from unity within $1 \leq \ell \leq 6$.

Detector limited acceptance, event multiplicities and detector efficiency all have counter strategies. Then, with the method for angular power spectrum estimation established, it is time to move on to data.

III. APPLYING TO DATA

The correction methods described in the previous section successfully returned the expected average power spectra values in the low ℓ regime, i.e. $\ell \leq 6$. Given this result, we may confidently apply the latest discussed method to data itself. The first consideration is vertex selection, a feature not dealt with in Ref. [13]. Then, the corrected angular power spectrum $\langle S_\ell^{m \neq 0} \rangle$ for heavy-ion data is displayed for all centralities. The translation from power spectrum to flow is yet calculated again, since the resolution has changed. These values are also compared to v_n computations with an η gap. Lastly, the transverse momentum phase space is separated and each of their corresponding spectra calculated.

A. Vertex selection

When heavy ions collide in the ALICE detector, the resultant particles firstly reach the Inner Tracking System (ITS) of the experiment, a cylindrical detector whose main tasks consist in primary and secondary vertices reconstruction, aside from tracking and identification of particles [17]. This subsection essentially focuses on the location of each event's primary vertex, or interaction point, and how the resulting power spectrum changes when selecting the position where the collision occurred and then following the steps depicted on previous sections.

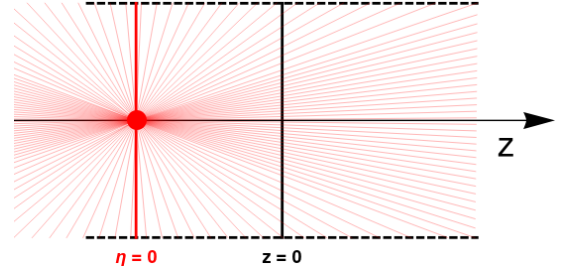


FIG. 7. Scheme of a heavy ion collision whose primary vertex is located at $z = -7.5$ cm

The interaction point of an event may be located anywhere along the beam axis z spanning a couple of centimeters along the interaction region. For the data set at hand, each collision happened in the interval -10 cm $< z < 10$ cm, where $z = 0$ cm is in the center of the ITS detector, represented by a thick black line in Fig. 7. The latter shows an schematic representation of the ITS' cross section. At mid-rapidity, i.e. $\eta = 0$, the collision happens: the lines coming out of it crudely represent the resultant particles, whose directions of emission span over the whole pseudorapidity (or θ) and azimuthal ranges. However, with the primary vertex located at, for instance, $z_{vtx} = -7.5$ cm and the detector's coverage limited to the dashed lines in Fig. 7, particles with $0 > \eta > -0.9$ may end up not being tracked. Lastly, Fig. 8 illustrates how events (N_{evts}) from the given run are distributed along the vertex: note how their bulk is located near the center, i.e. $z = 0$ cm.

Both in the previous work [13] and up until this point in the current study, we have performed the full analysis, from mapping particles on Mollweide projections to correcting $\langle C_\ell^{m \neq 0} \rangle$ by multiplicity, on a batch of events whose interaction points were located anywhere along -10 cm $< z < 10$ cm. The objective of this section is then to first select in which interval with $dz = 2$ cm width the primary vertex is located. Secondly, the centrality division from 0-5% to 30-40% is determined and finally, the following steps are performed for each vertex interval: mapping particles, normalizing the event maps by $F^{all}(\mathbf{n}_p)$ and calculating their power spectra.

Events whose interaction points happen close to the

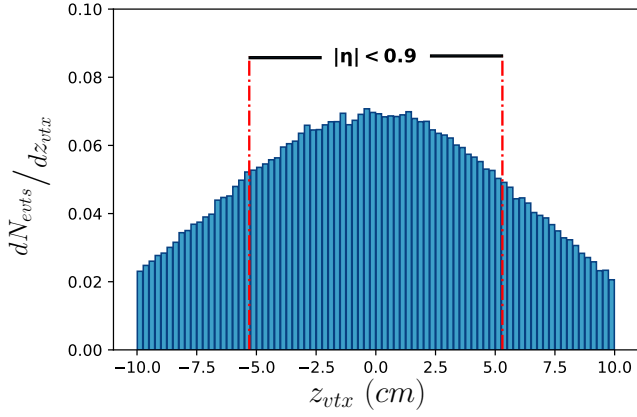


FIG. 8. Distribution of N_{evt} according to their z_{vtx} . The red lines indicate the z position where acceptance is uniform for $|\eta| < 0.9$.

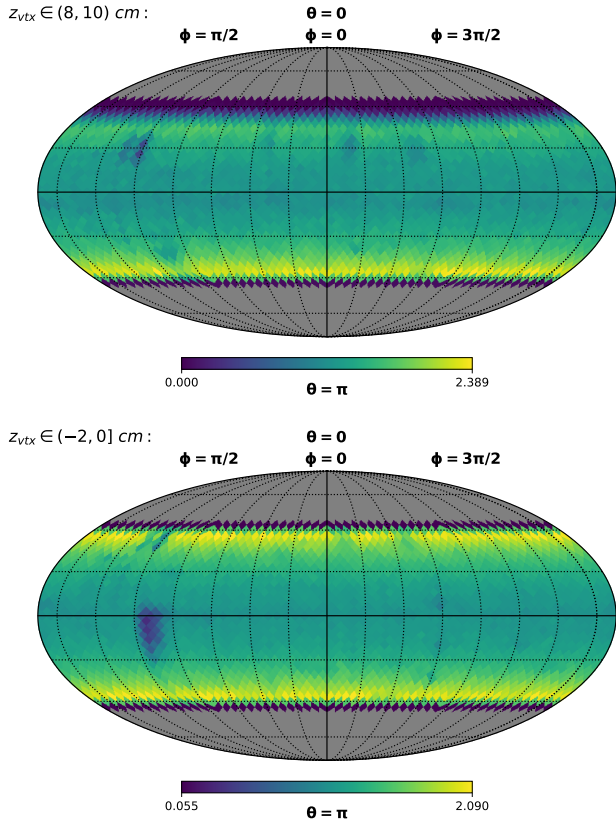


FIG. 9. $F^{all}(\mathbf{n}_p)$ for events with primary vertex in $(8, 10)$ cm (top) and $(-2, 0]$ cm (bottom). Maps are from the 10-20% centrality.

detector's edge, end up with unaccounted particles whose pseudorapidity lies within $|\eta| < 0.9$. Those escape the detector at only one of its sides, as illustrated in Fig. 7, which leads to an asymmetric θ distribution, shown on the top of Fig. 9. This map is the average over all events with primary vertex located within $(8, 10)$ cm: note its

asymmetry as pixels close to the top edge are not colored yellow, contrasting with the ones on the bottom.

On the bottom of Fig. 9 is the average over all event maps whose interaction point lies within $(-2, 0]$ cm of the detector center. It is one of the regions where majority of events happen. In contrast to the map on top, both edges are colored yellow, as they possess a similar number of particles per pixel. At this point, it is important to remark that even though these events are from the same run, both $F^{all}(\mathbf{n}_p)$ maps seem to have different detector-caused anisotropies. While for the one on top the inefficiency is located above $\theta = \pi/2$ ($\eta = 0$), for the other it is below. This suggests that the detector part responsible for the non-uniformity is located between the center and left edge of the interaction region. Unsurprisingly, the detector anisotropy seen in the mentioned maps also differ from the one seen on Fig. 4: as this map is a result of all events with primary vertices ranging from -10 cm to 10 cm and the non-uniformity ends up smeared over $|\eta| < 0.9$.

Due to the asymmetric geometry of the map from $(8, 10)$ cm, $a_{\ell 0}$ modes with ℓ odd are expected to be non-trivial. In order to verify that, distributions of $|a_{10}|^2$ from events of three vertex intervals were created. Their results are compared in Fig. 10, where it is clear to see that for $(8, 10)$ cm, its $|a_{10}|^2$ values spam over three orders of magnitude. Meanwhile, for $(-2, 0]$ cm their average lies in $\mathcal{O}(10^{-3})$, the expected value for fully isotropic distributions with these multiplicity values.

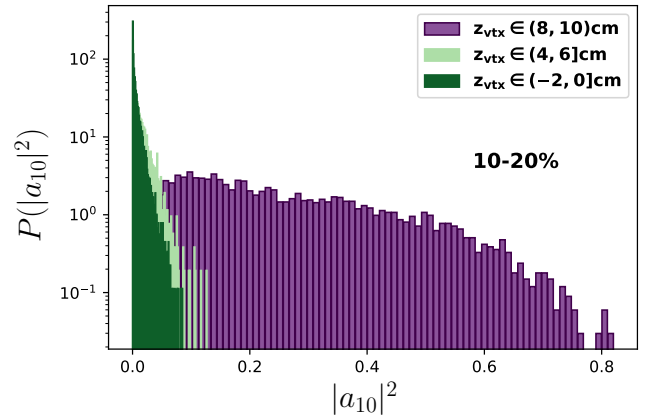


FIG. 10. Distribution of coefficients $|a_{10}|^2$ for events with different vertex intervals.

In the previous study [13] the full averaged power spectra $\langle C_\ell \rangle$ with ℓ odd for different centralities were found to follow a power law behavior $C(\ell) = A \cdot \ell^{-\beta} + C$. Given how modes like a_{10} are highly altered due to the asymmetries, this power law behavior of $\langle C_\ell \rangle$ for odd ℓ is simply a combination of asymmetric maps in θ and their ϕ anisotropy.

B. Data spectrum

Finally we reach the point where we correct the spectra corresponding to each of the vertices, by subtracting $\langle N_\ell^{m \neq 0} \rangle$ from $\langle C_\ell^{m \neq 0} \rangle$. The $\langle C_\ell^{m \neq 0} \rangle$ we are interested in correcting corresponds to that of normalized maps, $\bar{f}(\mathbf{n}_p)$, whose anisotropies caused by detector efficiency should have been smoothed out. In this case, its averaged power spectrum should be subtracted by $\langle N_\ell^{m \neq 0} \rangle_{bar}$, calculated from data maps azimuthally randomized and normalized by their averaged map. This step is repeated for all intervals at hand separately and, at the end, the average over the intervals is taken, a quantity denoted by $\langle S_\ell^{m \neq 0} \rangle_z$.

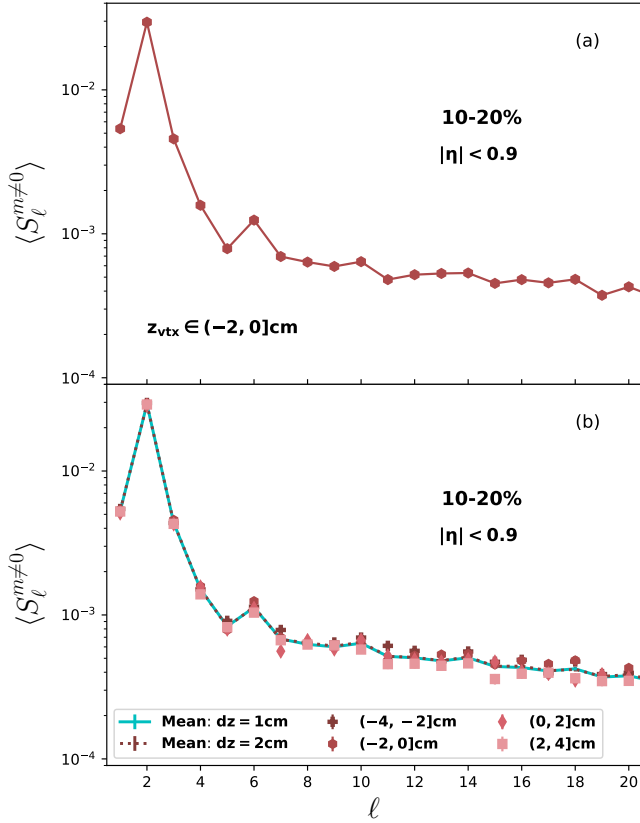


FIG. 11. Estimated $\langle S_\ell^{m \neq 0} \rangle$ for the interval $(-2, 0]$ cm (a). Corrected average spectra for each vertex interval and $\langle S_\ell^{m \neq 0} \rangle_z$ over all vertices for interval widths $dz = 1$ cm and $dz = 2$ cm (b).

In this study, particles emitted from events with z_{vtx} within different intervals are considered to be drawn from the same distribution $f(\hat{\mathbf{n}})$, but affected by distinct detector efficiency functions $D_z(\hat{\mathbf{n}})$, where the subscript z indicates that it is vertex dependent. For the current analysis, an interval width of $dz = 2$ cm was chosen to maximize the number of events per interval, while maintaining $D_z(\hat{\mathbf{n}})$ approximately the same for the sample. Additionally, a uniform acceptance within $|\eta| < 0.9$ is

only possible for vertices $|z_{vtx}| < 5.3$ cm [17]. That explains why the intervals in Fig. 11 (b) range from -4 cm to 4 cm.

The corrected average power spectrum for the 10-20% centrality and vertex interval $(-2, 0]$ cm is depicted in Fig. 11 (a). Notice that it possesses the same peak at $\ell = 6$ present in the MC simulated distributions. The higher peak at $\ell = 2$ is also unsurprisingly conserved, a possible sign of elliptic flow, as already mentioned. In addition, it has a damping tail with periodic ‘dips’ on every fourth mode counting from $\ell = 8$ until $\ell = 20$. As seen in the MC cases, a spectrum fully dominated by flow anisotropies should drop significantly from $\ell = 7$. This means the aforementioned tail suggests the presence of anisotropies yet unaccounted for, as it does not possess, for example, the ‘dip’ at $\ell = 8$ present on the MC simulations. Those modes are probably dominated by short-ranged non-flow effects, such as jet cones or resonance decays.

The spectra (lines) at Fig. 11 (b) are weighted averages over all vertex intervals. They are presented alongside $\langle S_\ell^{m \neq 0} \rangle$ for each of the intervals within $(-4, 4]$ cm with a $dz = 2$ cm width (markers). As a means of testing the efficiency of the power spectrum estimation method developed, $\langle S_\ell^{m \neq 0} \rangle_z$ was also calculated for vertices within $(-5, 5]$ cm with $dz = 1$ cm. It readily agrees with $\langle S_\ell^{m \neq 0} \rangle_z$ for $dz = 2$ cm, indicating the reliability of the method.

Following up on the vertex averaged spectrum of 10-20%, $\langle S_\ell^{m \neq 0} \rangle_z$ for $dz = 2$ cm is calculated for the remaining centralities 0-5%, 5-10%, 20-30%, and 30-40%. The current centrality division differs from the one in Ref. [13], due to maximization of N_{evts} after the separation in vertex intervals and p_T phase space. The resultant $\langle S_\ell^{m \neq 0} \rangle_z$ are shown in Fig. 12. At first glance, the usual features can be spotted: a peak at $\ell = 2$ followed by decreasing values until a peak at $\ell = 6$. For higher modes, a damping tail dominates the spectra. There is also a clear hierarchy between centralities.

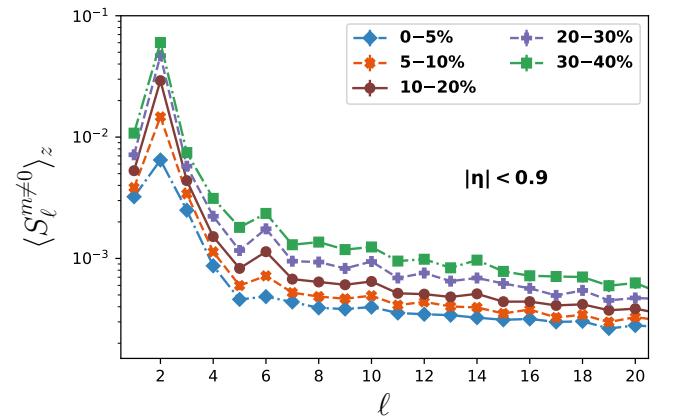


FIG. 12. Power spectra $\langle S_\ell^{m \neq 0} \rangle_z$, $dz = 2$ cm for centrality intervals 0-5%, 5-10%, 10-20%, 20-30%, and 30-40%.

All the spectra in Fig. 12 have the large-scale characteristics of a scenario with anisotropic flow, since for $\ell \leq 6$ they resemble the MC spectra in Fig. 3. Also, how their values increase with more peripheral centralities is akin to the behavior of azimuthal flow coefficients [23].

The angular power spectrum describes correlations between (θ, ϕ) pairs, so any phenomenon, from short to long-ranged, pertaining to two-particle correlations should contribute to $\langle S_\ell^{m \neq 0} \rangle_z$. That includes jets, hadron decays, quantum fluctuations, among others. Since these are short ranged, their presence could be the main cause of the damping tail of $\langle S_\ell^{m \neq 0} \rangle_z$.

C. From spectrum to azimuthal flow

In light of the current approach to calculate the angular power spectrum of heavy-ions, it has been deemed important to repeat the azimuthal flow extraction from Ref. [13]. Not only has the resolution changed, but the events at hand were selected with uniform acceptance within $|\eta| < 0.9$. In other words, effects from maps asymmetric around $\theta = \pi/2$ were eliminated. Furthermore, $D_z(\mathbf{n}_p)$ was considered for each vertex interval, thus assigning the corrected pixel weights from detector efficiency. We begin by finally presenting how azimuthal flow calculation works for MC simulations in comparison to the Q-cumulants method [24, 25] and then move on to the data spectra, where v_n will be also computed with an η gap.

From the flow ansatz, the azimuthal distribution of the emitted hadrons can be expanded in a Fourier series [26, 27]:

$$\frac{dN}{d\phi} \propto \frac{1}{2\pi} \left[1 + 2 \sum_{n=1}^{\infty} v_n \cos n(\phi - \Psi_n) \right], \quad (8)$$

where v_n are the azimuthal flow coefficients and Ψ_n are the symmetry planes associated with them. Consider now heavy ion events, from either simulations or real data, drawn from a factorizable distribution of the type $f(\hat{\mathbf{n}}) = g(\theta)h(\phi)$ as presented on the previous section. Additionally, take $h(\phi) = dN/d\phi$ as the flow ansatz in Eq. 8. From the expansion of $f(\hat{\mathbf{n}})$ in spherical harmonics [13]:

$$\begin{aligned} a_{\ell 0} &= b_{\ell 0} & \text{for } m = 0, \\ a_{\ell m} &= b_{\ell m} \cdot v_{|m|} e^{-im\Psi_{|m|}} & \text{for } m \neq 0, \end{aligned} \quad (9)$$

with

$$b_{\ell m} = N_{\ell m} \int_{\theta_i}^{\theta_f} g(\theta) P_{\ell m}(\cos \theta) \sin \theta d\theta, \quad (10)$$

where (θ_i, θ_f) correspond to $\eta = 0.9$ and $\eta = -0.9$, respectively. Additionally, $N_{\ell m}$ is the square root coefficient

of the spherical harmonics and $P_{\ell m}$ are the associated Legendre polynomials.

The azimuthal flow coefficients v_n are extracted by combining Eq.(9) with the expression in Eq.(4):

$$|v_n|^2 = \frac{2n+1}{2} \cdot \frac{C_n^{m \neq 0}}{|b_{nn}|^2} \cdot \frac{|b_{00}|^2}{C_0} \quad \text{or} \quad (11)$$

$$|v_n|^2 = \frac{1}{|b_{nn}|^2} \left[\frac{2n+1}{2} \cdot C_n^{m \neq 0} - \frac{2n-3}{2} \cdot \frac{|b_{n-2}|^2}{|b_{n-2n-2}|^2} \cdot C_{n-2}^{m \neq 0} \right] \frac{|b_{00}|^2}{C_0}, \quad (12)$$

where $|b_{00}|^2/C_0$ is a normalization factor. The expressions in Eqs.(11, 12) are valid for $n = 1, 2$ and $n = 3, 4$, respectively. It should also be remarked that the v_n coefficients are calculated from the averaged corrected spectrum $\langle S_\ell^{m \neq 0} \rangle$.

We begin by confirming whether or not they are valid for the simulated distribution drawn from $f_{MC}(\hat{\mathbf{n}})$, explicitly expressed by Eq.(5). The objective consists in recovering the input v_n values from the power spectrum alone, here denoted as $v_n\{C_\ell\}$, and compare them to the Q-cumulants' result for 2-particle correlations, denoted as $v_n\{2, QC\}$ or $v_n\{2\}$. The simulations have the same multiplicity as each of the centralities from 0-5% to 30-40% with v_n input values that increase as collisions become more peripheral. Flow coefficients are also computed from $\bar{f}_{D_2}(\mathbf{n}_p)$, as said maps are closer in similarity to the data ones.

It is clear to see in Fig. 13 that getting azimuthal coefficients from the power spectrum through Eqs (11, 12) works perfectly for the MC simulations. The resulting v_n values are within error of the input ones and of the Q-cumulants' method. Even the coefficients from $\bar{f}_{D_2}(\mathbf{n}_p)$ (stars) for centralities 0-5%, 10-15% and 35-40% describe the input values. Given that these MC distributions are purely dominated by flow, the result is not surprising.

As the extraction of flow coefficients through $\langle S_\ell^{m \neq 0} \rangle$ works well for the MC-simulated emitted particles, the same steps were applied to the normalized maps of public data. The v_n coefficients were calculated using Eqs.(9, 10) for $b_{\ell m}$ from $g(\theta)$ as a constant, due to the normalization of data maps by their average θ distribution. This power spectrum estimation of azimuthal flow was compared again to the Q-cumulants method for two-particle correlations, now denoted $v_n\{2\}$. In addition to the latter, a pseudorapidity gap of $\Delta\eta > 1$ was imposed in order to suppress non-flow effects, this approach is denoted as $v_n\{2, \Delta\eta > 1\}$.

A trend can be observed in Fig. 14: flow coefficient values calculated using the power spectrum are typically higher than their Q-cumulants counterparts. This same effect had already been observed in Ref. [13] using $N_{side} = 8$ without accounting for the anisotropies from vertex selection. It is not surprising that $v_n\{C_\ell\}$ should stand above $v_n\{2, \Delta\eta > 1\}$, since the latter does not

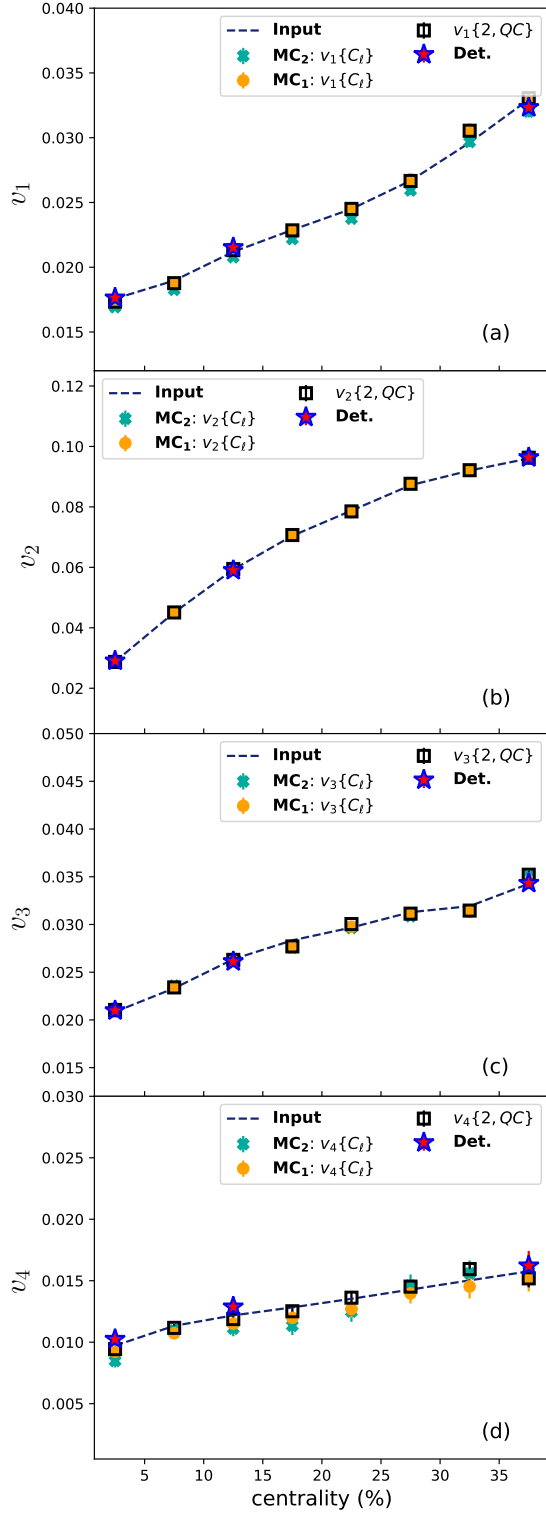


FIG. 13. Comparison between the power spectrum extraction $v_n\{C_\ell\}$ and Q-cumulants $v_n\{2, QC\}$ to the input values of v_n , for $n = 1, \dots, 4$.

consider short-ranged particle correlations in η . However, there is a difference between $v_n\{C_\ell\}$ and $v_n\{2\}$ de-

spite the MC results suggesting that given a function $f(\hat{\mathbf{n}}) = g(\theta)h(\phi)$ they should be the same. In conclusion, the assumption that data follows a factorizable function even within $|\eta| < 0.9$ should be regarded carefully.

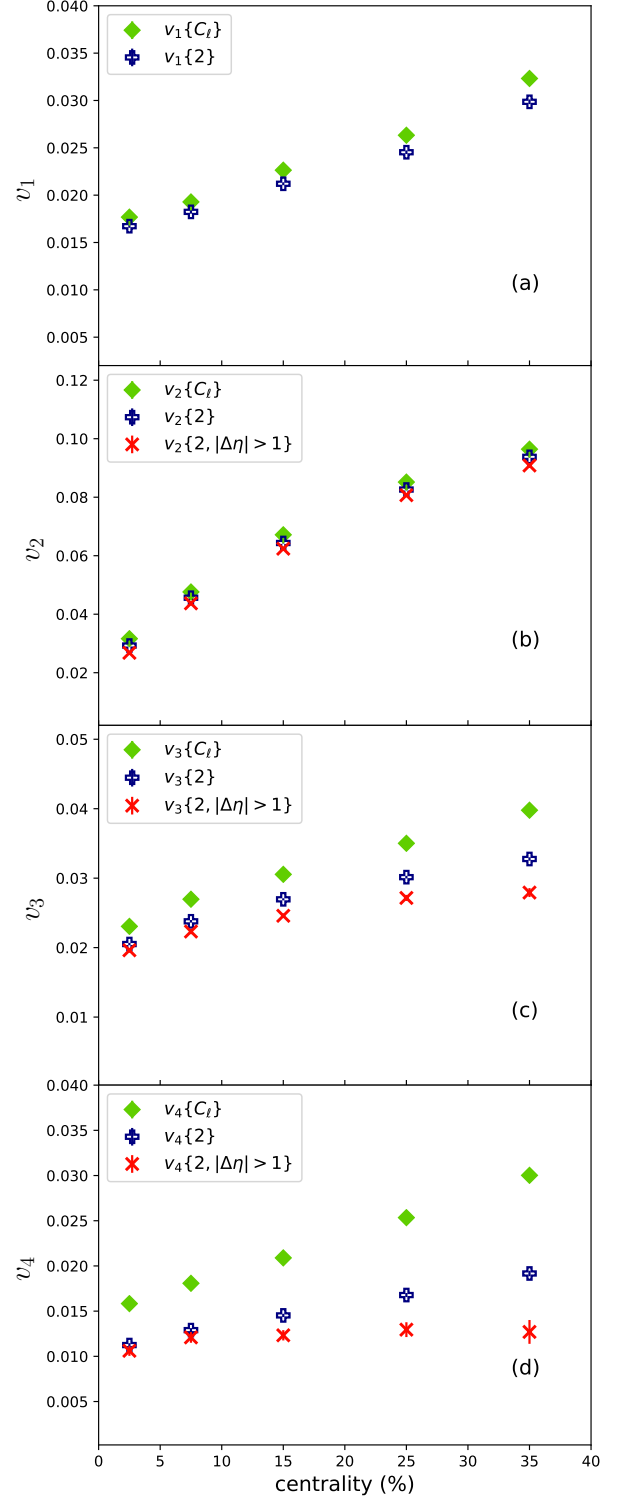


FIG. 14. Comparison between power spectrum and Q-cumulants method for extraction of v_n for data.

Alternatively, consider the final event distribution as a superposition of maps: one with the large scale structures and another with the short-ranged ones. When computing the power spectrum, their final harmonic coefficients $|a_{\ell m}|^2$ would receive contributions not only from the single maps $|a_{\ell m}^A|^2$ and $|a_{\ell m}^B|^2$, but also from their cross-term $a_{\ell m}^A (a_{\ell m}^B)^* + (a_{\ell m}^A)^* a_{\ell m}^B$. Here A and B represent the large and small-scale structure maps.

Yet another way of understanding the difference between $v_n\{C_\ell\}$ and $v_n\{2\}$ is to consider that the 3-D geometry of non-flow anisotropies is seen differently through spherical and azimuthal two-particle correlations. Lastly, the result of $v_n\{2, \Delta\eta > 1\}$ for $n = 1$ indicates that the values of v_1 are short-ranged in η , i.e., not an anisotropy related to a symmetry plane Ψ_1 . For instance, single jets could contribute to the high dipole.

D. Transverse momentum

In the previous sections, we showed that the average angular power spectrum from total multiplicity maps contains a non-trivial large-scale structure which is probably related to the extensively studied flow coefficients. It also has a damping tail, associated to short-ranged two-particle correlations. When comparing calculations of v_n through $\langle S_\ell^{m \neq 0} \rangle_z$ and the well known Q-cumulants method for the ALICE data, however, we found discrepancies between all flow harmonics, suggesting that $f(\hat{\mathbf{n}}) \neq g(\theta)h(\phi)$.

Correlations between produced particles in heavy ion collisions are also studied as a function of transverse momentum, p_T [23]. Additionally, the dependence of v_n coefficients on p_T also provides information on the hydrodynamical behavior of the QGP, aside from being sensitive to the medium's viscosity [7]. In light of these, we study now how multiplicity maps and their spectra change with transverse momentum.

The objective in this section is to make a simple, yet straightforward analysis of how the angular power spectrum changes with p_T . Therefore, we begin by separating the resulting particles of each event in two transverse momentum intervals: $p_T < 0.54$ GeV, or *lower* p_T , and $p_T > 0.54$ GeV, or *upper* p_T . The choice of such intervals results in each of their events having approximately the same multiplicity.

After separating the particles of each event by their p_T values, we perform the usual step of making their multiplicity maps by projecting their angular coordinates (θ_i, ϕ_i) onto a sphere. Then a background spectrum $\langle N_\ell^{m \neq 0} \rangle$ is estimated for both of them separately and subtracted from their spectra ensemble averages. Finally, the weighted average of the vertex spectra is taken, yielding $\langle S_\ell^{m \neq 0} \rangle_{Uz}$ for $p_T > 0.54$ GeV and $\langle S_\ell^{m \neq 0} \rangle_{Lz}$ for $p_T < 0.54$ GeV.

The maps under full momentum phase space studied so far can be seen as the superposition of a map whose particles have $p_T > 0.54$ GeV and another whose par-

ticles have $p_T < 0.54$ GeV. The $a_{\ell m}$ of the full phase space map has the following relation to the harmonic coefficients of the aforementioned maps:

$$|a_{\ell m}|^2 = |a_{\ell m}^U|^2 + |a_{\ell m}^L|^2 + (a_{\ell m}^U)^* \cdot a_{\ell m}^L + a_{\ell m}^U \cdot (a_{\ell m}^L)^*, \quad (13)$$

where $a_{\ell m}^U$ and $a_{\ell m}^L$ correspond, respectively, to the upper and lower bounds of the p_T intervals.

The terms in Eq. (13) can be summed in m for all ℓ and divided by $2\ell + 1$, showing that the spectra from Fig. 12 are equal to the sum of $\langle S_\ell^{m \neq 0} \rangle_{Uz}$ and $\langle S_\ell^{m \neq 0} \rangle_{Lz}$ plus a cross-term. Those three are depicted in Fig. 15 for the 10-20% centrality.

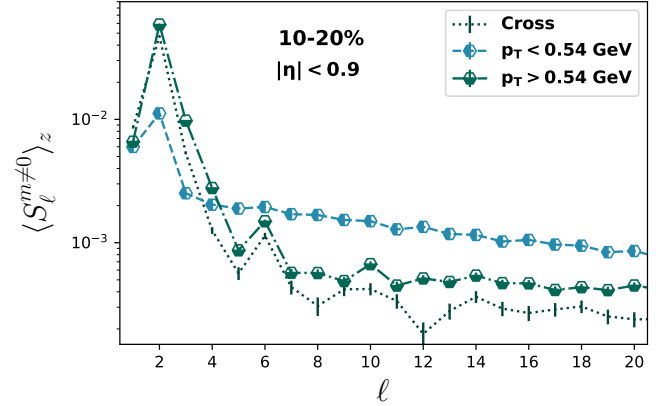


FIG. 15. Estimated $\langle S_\ell^{m \neq 0} \rangle_z$ for lower, upper p_T and their cross-term at 10-20% centrality.

Note from Fig. 15 how the spectra for $p_T > 0.54$ GeV and $p_T < 0.54$ GeV retained different characteristics after correction. Firstly, upper- p_T has a more typical flow-dominated shape, with not only the peak in $\ell = 2$ and $\ell = 6$, but also $\ell = 10$, an effect highly influenced by v_2 . Additionally, it has also a higher value at $\ell = 3, 4$ than its counterpart. In turn, the power spectrum at lower- p_T dominates the picture for $\ell \geq 5$ and it possesses a seemingly more slanted damping tail than the ones present in Figs. 11, 12.

From Fig. 15, it can be seen that particles with higher momentum encode most of the anisotropies arising from fluctuations in initial conditions, given how $\langle S_n^{m \neq 0} \rangle_{Uz}$ for $\ell = 2, 3$ stand way above their lower momentum counterparts. This observation is in agreement with measurements of $v_n(p_T)$, which show that flow coefficients have higher values with increasing p_T [23].

The cross-term (dashed line) in Fig. 15 has similar shape compared to $\langle S_n^{m \neq 0} \rangle_{Uz}$. Interestingly, the cross-term does not need correction for multiplicity, since the backgrounds of each p_T spectrum are independent quantities, i.e., not correlated to each other.

On the follow-up, the averaged spectra for upper- and lower- p_T intervals are calculated for all centralities. The result is shown in Fig. 16 for $p_T > 0.54$ GeV (a) and

$p_T < 0.54$ GeV (b). Overall, the centrality hierarchy remains, with spectrum values increasing as collisions become more peripheral. Next, we tackle the characteristics of each spectrum separately.

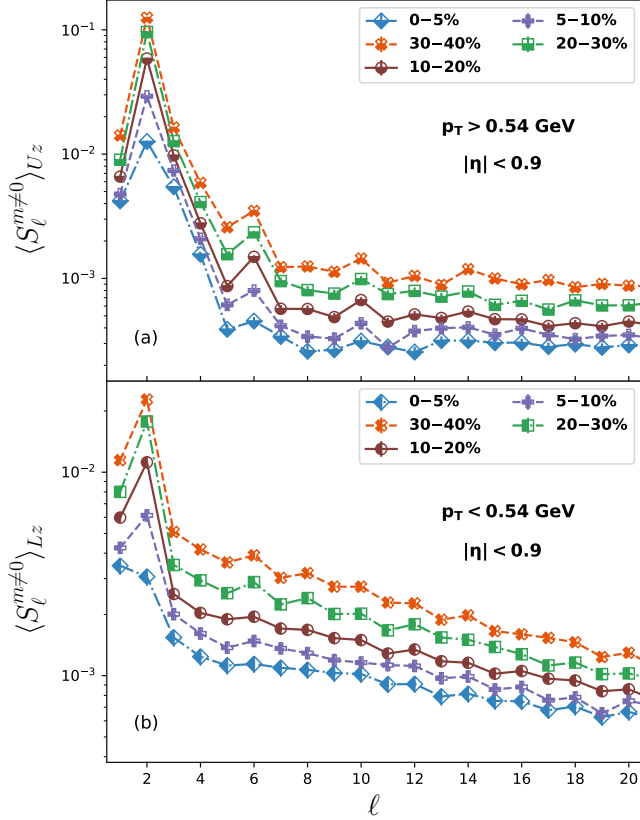


FIG. 16. Angular power spectra of distributions with $p_T > 0.54$ GeV (a) and $p_T < 0.54$ GeV (b) as they change with centrality.

The features of $\langle S_\ell^{m=0} \rangle_{Uz}$ are quite sharp at $\ell \leq 6$, with values flattening out at higher ℓ . The clear exception is $\ell = 10$, which suggests an increase in dominance of initial conditions anisotropies. The aforementioned plateau at higher ℓ indicates that the size of fluctuations does not change significantly with scale from $\ell = 11$.

In the case of $\langle S_\ell^{m=0} \rangle_{Lz}$ it is now clear to see that the damping tails have become more slanted than in the full p_T phase space spectra. Meanwhile, the peak at $\ell = 6$ has been smoothed out, though the one at $\ell = 2$ has remained for all but 0-5%. The relatively high $\ell = 2$ suggests that these low momentum particles are globally arranged like the initial overlapping region. Said particles are associated with small-scale phenomena, which is hinted at by the surpassing $\ell = 1$ mode over $\ell = 2$ for 0-5%.

Since the tails of $\langle S_\ell^{m=0} \rangle_{Uz}$ seem to decay with a power-law, a fit to the function $P_{ow}(\ell) = \mathcal{A} \cdot \ell^\gamma$ was performed to the modes with $3 \leq \ell \leq 20$ on the spectra of all centralities. Due to \mathcal{A} being just a scaling factor, only

the exponent γ was plotted as a function of centrality.

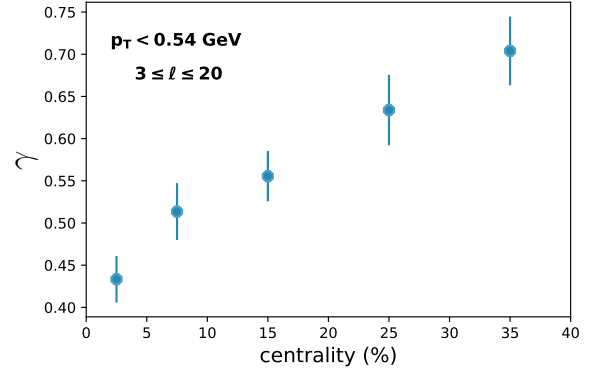


FIG. 17. Power-law exponent γ as it changes with centrality.

It can be observed from Fig. 17 that γ increases with centrality percentile. This means that the tails in Fig. 16 (b) decrease faster for more peripheral collisions. One could consider the rarefaction of the medium: central events would have more particle clusters at smaller scales than peripheral ones, as their number of participants would allow for less particles being produced.

Taking the geometry of momentum conservation to mean particles emitted on opposite sides of a sphere, it is possible to see that only $Y_{\ell m}$ with even ℓ have such symmetry. As a consequence, an spectrum influenced by momentum conservation would possess enhanced even modes. This effect can be slightly seen in the $\langle S_\ell^{m=0} \rangle_{Lz}$ of 20-30% and 30-40% centralities. The sparsity in the medium of events belonging to these centralities allow for particles to travel without interacting much after hadronization.

The relatively high dipole moment ($\ell = 1$) persisted in all spectra seen in this work. This large-scale geometry is connected to Y_{11} and Y_{1-1} , which suggests a net asymmetry in ϕ . Also, from the results of $v_n\{2, \Delta\eta > 1\}$, this anisotropy is short-ranged in θ . A possible explanation could be a jet emitted on one direction, while its partner got swallowed by the medium.

E. Model comparison

The averaged power spectra over distinct vertex intervals $\langle S_\ell^{m=0} \rangle_z$ for both full- p_T phase space and the intervals $p_T < 0.54$ GeV and $p_T > 0.54$ GeV have been displayed for heavy-ion data at $\sqrt{s_{NN}} = 2.76$ TeV measured with the ALICE detector. The results contain features associated with different sources of two-particle correlations, where global geometries arising from initial conditions dominate the low- ℓ region and phenomena unrelated to flow should be prominent in the high- ℓ region.

Given characteristics such as the peaks in $\ell = 2$ and $\ell = 6$, as well as the damping tail from $\ell = 3$ in the spectra for $p_T < 0.54$ GeV, a comparison to well-established

models of heavy-ion collisions is a necessary step in this exploration of the angular power spectrum. Since spherical projections of data require knowing the final particle distribution both in the longitudinal and transverse directions, it is adamant to employ a 3+1D model.

A multi-phase transport model AMPT [16] explicitly handles non-equilibrium many-body dynamics. Overall, it consists of four main stages: initial conditions, parton dynamics, hadronization and hadronic interactions. Strings and minijets dominate the initial state, which is modeled with the heavy-ion jet interaction generator (HIJING) [28–31]. In the string melting [32–34] version of AMPT, excited strings are converted to partons according to their valence quarks. Then, the space-time evolution of the initial partons is treated with Zhang’s parton cascade (ZPC) [35]. Subsequently, hadronization is described by a quark coalescence model which combines partons into hadrons. Finally, the latter’s interactions are defined by a relativistic transport (ART) [36, 37] model for hadrons.

The AMPT version employed in this study was *v2.26t7b* with a string melting mechanism, released on May of 2018. The model was run for Pb-Pb collisions at center-of-mass energy per nucleon $\sqrt{s_{NN}} = 2.76$ TeV. The choice of parameters followed Ref. [38] and the resulting simulated particles reproduce mid-pseudorapidity and transverse momentum charged-particle distributions of ALICE heavy-ion data. Explicitly, the values for the screening mass and strong coupling constant are, respectively, $\mu = 2.265 \text{ fm}^{-1}$ and $\alpha_s = 0.33$, which correspond to a parton cross-section of 3 mb. In addition, the Lund string fragmentation parameters used are $a = 0.3$ and $b = 0.15 \text{ GeV}^{-2}$.

In this study, the AMPT power spectra are compared to ALICE data for a single centrality window, 10-20%. The estimation of impact parameter values followed the expression $c \simeq \pi|\mathbf{b}|^2/\sigma_{in}$ [39], where c stands for centrality, \mathbf{b} is the impact parameter and $\sigma_{in} \approx 784 \text{ fm}^2$ the nucleus-nucleus total inelastic cross-section calculated from the Glauber model. For the 10-20% most central events, the minimum and maximum impact parameter values were thus 5.0 fm and 7.1 fm, respectively.

Around 7000 AMPT events were generated with random symmetry plane orientations for the 10-20% centrality. Single event maps $f_{sim}(\mathbf{n}_p)$ for each of these events were then created for particles with $|\eta| < 0.9$. Likewise experimental data, an all-event map $F_{sim}^{all}(\mathbf{n}_p)$ was created from the overlap of all ~ 7000 $f_{sim}(\mathbf{n}_p)$ maps. Since AMPT particle distributions are ‘measured by a perfect detector’, $D_{sim}(\mathbf{n}_p) = 1$ and the all-event map is simply the average θ -distribution, $F_{sim}^{all}(\mathbf{n}_p) = g_{sim}(\mathbf{n}_p)$, in accordance to Eq. 6. Following the steps of ALICE data spectrum we calculate $\bar{f}_{sim}(\mathbf{n}_p) = f_{sim}(\mathbf{n}_p)/F_{sim}^{all}(\mathbf{n}_p)$ in analogy to Eq. 7.

The resulting maps $\bar{f}_{sim}(\mathbf{n}_p)$ have assigned pixel weights according to the average θ -distribution of AMPT events, which should agree with ALICE data given how both pseudorapidity distributions are consistent within

$|\eta| < 0.9$. The angular power spectra of AMPT are then calculated from $\bar{f}_{sim}(\mathbf{n}_p)$ and their average multiplicity background $\langle N_\ell^{m \neq 0} \rangle_{sim}$ is estimated in the same manner as done for the ALICE data itself. Specifically, 10^6 events following the AMPT θ -distribution, $g_{sim}(\mathbf{n}_p)$, and uniform in ϕ were generated. Their multiplicities reflected those of the AMPT events themselves. Each created event map was then divided by $g_{sim}(\mathbf{n}_p)$ to assign pixel weights which match those of the AMPT maps. Their spectra were calculated and averaged over yielding $\langle N_\ell^{m \neq 0} \rangle_{sim}$.

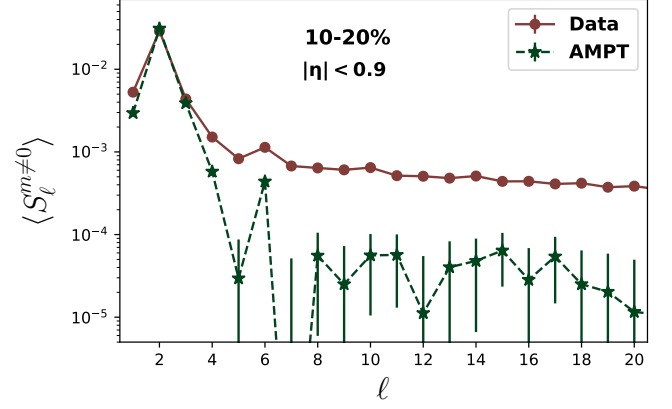


FIG. 18. Comparison between averaged power spectra $\langle S_\ell^{m \neq 0} \rangle$ from ALICE data and AMPT model.

The resulting averaged angular power spectrum of AMPT events $\langle S_\ell^{m \neq 0} \rangle_{sim}$ is depicted in Fig. 18. Additionally, it is compared to the ALICE data spectrum $\langle S_\ell^{m \neq 0} \rangle_z$ for the 10-20% centrality. Note how the AMPT spectrum reasonably matches data for $\ell = 2, 3$. More specifically, $\langle S_\ell^{m \neq 0} \rangle_{sim}$ is within 6.5% and 11.2% of the data spectrum values for $\ell = 2$ and $\ell = 3$, respectively.

Given the aforementioned result, the next step consisted in estimating v_n for AMPT using both Q-cumulants and C_ℓ - Eqs. (11, 12). Recall from Fig. 14 that, in the ALICE data case, $v_n\{2\}$ and $v_n\{C_\ell\}$ diverge from each other specially for $\ell > 2$. As means of quantifying the differences between both v_n calculations, we compute $|1 - v_n\{2\}/v_n\{C_\ell\}|$ for both the experimental data and AMPT.

The relative difference between Q-cumulants and C_ℓ on the ALICE data case more than doubles as n increases, with $v_n\{C_\ell\}$ always yielding a higher value than $v_n\{2\}$; see Fig. 14. On the other hand, $v_n\{C_\ell\} < v_n\{2\}$ for $n = 3, 4$ in the AMPT case. Additionally, the simulation’s result $|1 - v_4\{2\}/v_4\{C_\ell\}| \approx 0.072 \pm 0.066$ was the highest among $n = 2, 3, 4$, with the others lying below 0.02. In other words, both Q-cumulants with two-particle correlations and the power spectrum estimations of v_n yield the same results in the AMPT case. A feature not present in the experimental data.

All in all, the AMPT spectrum reproduces the shape

of the ALICE data spectrum until $\ell = 6$. Beyond this multipole value, $\langle S_\ell^{m \neq 0} \rangle_{sim}$ is, on average, a full order of magnitude below data and has a shape more indicative of an isotropic spectrum. An increase in number of events could aid in defining the shape better, though it is unlikely that it would match the data spectrum.

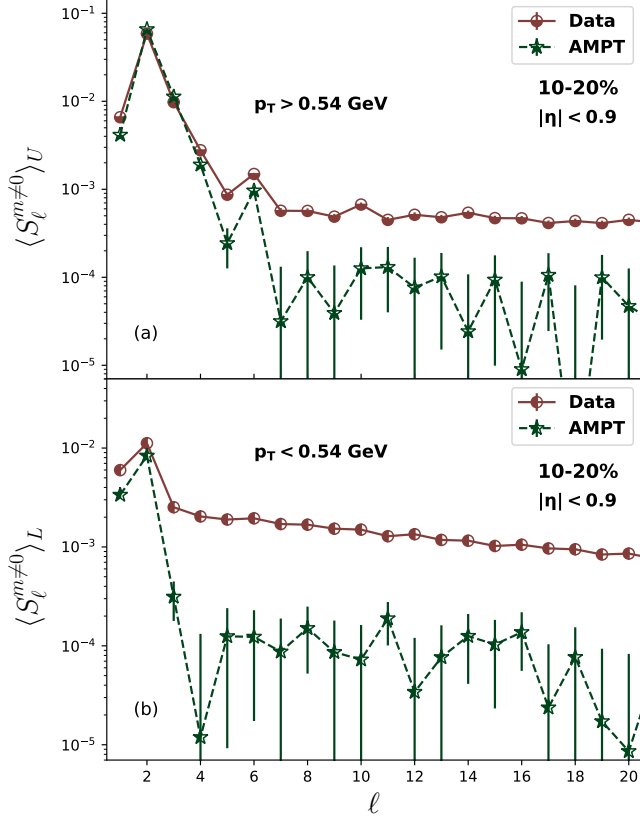


FIG. 19. Angular power spectra of ALICE data and AMPT model for $p_T > 0.54$ GeV (a) and $p_T < 0.54$ GeV.

Likewise the full- p_T phase space case above, AMPT angular power spectra are also calculated for the transverse momentum intervals $p_T > 0.54$ GeV and $p_T < 0.54$ GeV. The events pertain to the same batch presented before, within the 10-20% centrality class. We follow the same steps described before: create event maps, divide each by the total ensemble sum, calculate their spectra and take their average. In order to estimate the background, create 10^6 events with $g_{sim}(\mathbf{n}_p)$ as their θ -distribution and uniform in ϕ . Divide each event by $g_{sim}(\mathbf{n}_p)$, calculate their spectra and average over them, finally yielding $\langle N_\ell^{m \neq 0} \rangle_{sim}$ for each p_T interval.

The corrected spectra for $p_T > 0.54$ GeV and $p_T < 0.54$ GeV are shown in Fig. 19 (a) and (b), respectively. They are compared to the data spectra for 10-20% already presented in Fig. 16. The AMPT power spectra for the upper and lower p_T bounds shall be denoted $\langle S_\ell^{m \neq 0} \rangle_U^{sim}$ and $\langle S_\ell^{m \neq 0} \rangle_L^{sim}$, respectively.

In the case of $p_T > 0.54$ GeV, a proximity of

$\langle S_\ell^{m \neq 0} \rangle_U^{sim}$ to the data spectrum for $\ell = 4, 5, 6$ is observed. Similarly to Fig. 18, AMPT describes the shape of the spectrum until $\ell = 6$. There is no peak at $\ell = 10$, a feature that becomes prominent when the transverse momentum phase space is sliced. Instead, for $\ell > 6$ $\langle S_\ell^{m \neq 0} \rangle_U^{sim}$ stands closer to the MC cases above than experimental data. There is no coherent pattern, which suggests that at such scales, AMPT particle distributions are nearly isotropic.

As for $p_T < 0.54$ GeV, $\langle S_\ell^{m \neq 0} \rangle_L^{sim}$ at $\ell = 2$ remains enhanced relative to the other multipoles, indicating the presence of an overall geometry connected to the initial overlapping region. On the other hand, higher ℓ possess the same behavior as previous spectra: no significant pattern and large error bars. This enforces the idea that AMPT within the current settings has no specific small scale structure. Meanwhile, the data spectra have a damping tail which becomes more slanted with peripheral collisions.

Lastly, the AMPT spectra also have an azimuthal asymmetry short-ranged in η . This is further supported by the non-zero $v_1\{2\}$, the Q-cumulants estimation without η -gap.

IV. DISCUSSION

This work explored two-particle correlations on a sphere, while it aimed at furthering our knowledge on anisotropies along the beam axis. The method presented in Ref. [13] was firstly detailed and applied to Monte Carlo simulated distributions in a pure flow scenario. Possible issues arising from limited detector acceptance and efficiency, as well as event multiplicity were properly tackled. Overall, the resulting spectra managed to describe the distributions up until an angular scale corresponding to $\ell = 10$.

Once the method of power spectrum estimation had been established, it was applied to ALICE data. Considerations on the vertex position of each event had to be made, since for $|z_{vtx}| > 5.3$ cm acceptance for $|\eta| < 0.9$ is non-uniform and gives rise to artificial anisotropies; e.g. the power law behavior of uncorrected odd modes [13]. Given a vertex interval, events were classified in the following centralities: 0-5%, 5-10%, 10-20%, 20-30%, and 30-40%. Their observed and background power spectra were calculated and their averages subtracted from each other, yielding $\langle S_\ell^{m \neq 0} \rangle$. Lastly, the latter's weighted average over all vertices was taken, resulting in Fig. 12.

The most striking characteristic of $\langle S_\ell^{m \neq 0} \rangle_z$ is the peak at $\ell = 2$, a clear signal of the initial almond shape imprinted in the final distribution. Additionally, the similarity to the MC spectra in a pure flow scenario indicates that primordial fluctuations are dominant in the region of large-scale structures, $\ell \leq 6$. The exception is $\ell = 1$, whose anisotropies are not related to a symmetry plane Ψ_1 .

Since $\langle S_\ell^{m \neq 0} \rangle_z$ encompasses azimuthal anisotropies, v_n

were calculated using it through Eqs. (11,12) and compared to two-particle correlation calculations with and without an η gap. Unsurprisingly, $v_n\{2, \Delta\eta > 1\}$ yielded lower values than the other two, due to suppression of non-flow effects. On the other hand, $v_n\{C_\ell\}$ remained higher than $v_n\{2\}$, suggesting that the assumption of data following a function $f(\hat{\mathbf{n}}) = g(\theta)h(\phi)$ might be insufficient, i.e., it could be true only on a first order approximation. Also, v_n and Ψ_n were taken to be approximately constant in θ . Their variation with the polar angle could be a possible explanation for the difference between $v_n\{C_\ell\}$ and $v_n\{2\}$.

The hierarchy $\langle S_2^{m \neq 0} \rangle_z > \langle S_3^{m \neq 0} \rangle_z > \langle S_4^{m \neq 0} \rangle_z$ is akin to that of v_n coefficients with $n = 2, 3, 4$. The increase of $\langle S_\ell^{m \neq 0} \rangle_z$ values with centrality percentile is also similar to that of azimuthal flow coefficients. These are part of the body of evidence pointing towards geometries of initial conditions being imprinted on the angular power spectrum.

It is with the exploration of the power spectra for different transverse momentum intervals that distinct geometries emerge. For instance, $\langle S_\ell^{m \neq 0} \rangle_{Uz}$ possesses higher values for $\ell \leq 4$ in comparison to $\langle S_\ell^{m \neq 0} \rangle_{Lz}$, while the latter dominates for $\ell > 5$. This can be explained due to $v_n(p_T)$ being higher for $p_T > 0.54$ GeV than for $p_T < 0.54$ GeV.

The spectrum $\langle S_\ell^{m \neq 0} \rangle_{Uz}$ has a peak in $\ell = 10$ in all centralities but 0-5%, its values until $\ell = 6$ are also higher than the full spectrum. Additionally, its shape resembles more that of the presented MC spectra, strongly suggesting the influence of initial geometries in its features. Taking a look at the angular two-particle correlation functions $C(\Delta\phi, \Delta\eta)$ [40], small-range correlations $(\Delta\phi, \Delta\eta) \approx 0$ also influence $p_T > 0.54$ GeV. The peak associated with these increases in value with centrality percentile. Also, it provides a reasonable explanation for the flattening out of the spectrum at $\ell > 10$, since the Fourier transform of a Dirac delta is a constant.

For particles with $p_T < 0.54$ GeV, $v_n(p_T)$ has relatively low values [23], implying that for $\langle S_\ell^{m \neq 0} \rangle_{Lz}$ the influence of primordial anisotropies dwindles significantly. Therefore, one could say that $\langle S_\ell^{m \neq 0} \rangle_{Lz}$ is mainly a spectrum of non-flow. For instance, the enhanced even modes for $6 \leq \ell \leq 12$ in the centralities 20-30% and 30-40% suggest that $Y_{\ell m}$ with ℓ even have a considerable contribution to the spectrum. These are characterized by symmetries between points diametrically opposed, which could imply momentum conservation.

The damping tail present on the CMB spectrum is caused mainly by photon diffusion, as these traveled from hot to cold areas of the universe, thus making it more uniform [41]. In other words, the scale of the fluctuations in the tail are comparable to the mean-free-path of photons. If the same interpretation is brought to the power spectra of heavy ions, then the observed suppression of higher ℓ modes indicates the length of mean-free-path l_{mpf} . What is more, l_{mpf} would depend on the trans-

verse momentum phase space, as the spectra for full- p_T , lower- p_T and upper- p_T differ from each other.

The comparison to AMPT showed that, under the current settings, the transport model managed to reproduce the shape of the data spectrum at $\ell \leq 6$ for both the full transverse momentum phase space and for $p_T > 0.54$ GeV. The enhancement of the dipole ($\ell = 1$) and quadrupole ($\ell = 2$) moments is present on all three AMPT spectra, with the first indicating an overall asymmetry in ϕ , though unrelated to a symmetry plane Ψ_1 . As for the second, it consists of an imprint of the almond-shaped geometry generated by the overlapping nuclei.

Despite the similarities described above, AMPT fails to emulate the data spectra for $\ell \geq 7$, in the cases of $\langle S_\ell^{m \neq 0} \rangle_{sim}$ and $\langle S_\ell^{m \neq 0} \rangle_U^{sim}$. For $p_T < 0.54$ GeV, the discrepancy starts at $\ell = 3$, as AMPT completely lacks a damping tail. All in all, beyond these scales dominated by initial stage fluctuations, or flow, the AMPT spectra values have no distinct feature. One could say the AMPT particle distributions look isotropic when probed at smaller scales.

Overall, AMPT underestimates the size of fluctuations on particle distributions. Specially when it comes to short-ranged scales, where AMPT's particles seem to be nearly isotropic, i.e., they follow no specific pattern. In other words, the AMPT model results in smoother particle distributions, while experimental data is lumpier.

Considering the possible relation between the heavy-ion angular power spectrum and the system's mean-free-path, AMPT could have a larger l_{mpf} than the experimental data. Specifically, one could think that the propagation of anisotropies to the final state is related to the mean-free-path. If the probed scale is bigger than l_{mpf} , than its patterns should be imprinted in the final distribution. However, if the opposite is true and l_{mpf} is actually larger than the scale in consideration, then the latter's characteristics will be smoothed out. Hence the AMPT spectra being more suppressed relative to the ALICE data.

Given the comparison to the AMPT model and possible relations to the mean-free-path of the system, it would be interesting to submit results from hydrodynamic 3+1D simulations to the power spectrum analysis present in this study. One could also verify how different stages of the QGP creation and evolution affect the angular power spectrum.

One of the main limitations of the developed method lies in the event multiplicities. With less particles, resolution should decrease, thus making the calculation of $a_{\ell m}$ less accurate. Analysis in the momentum range $p_T > 2$ GeV, or of different particle species and small collision systems are highly limited. Precisely due to the latter, the task of separating the different causes of anisotropies could be challenging.

This work adds to previous ones [42–44] in power spectrum analysis of heavy-ion collisions and it differs primarily from them due to its thorough exploration of modes with $m \neq 0$. It also tackles the relation between angu-

lar power spectrum and transverse momentum differently than Ref. [43]. In the latter, the pixels on the map correspond to p_T values themselves, with the power spectrum measuring correlations between $\Delta p_T/p_T(\hat{n})$ pairs. In the present work, the spectra at distinct p_T intervals still measures correlations between (θ, ϕ) pairs. Also, a depression in $\ell = 6$ was observed in the spectra of Ref. [43], while $\langle S_\ell^{m \neq 0} \rangle_z$ displays the exact opposite, an influence of the initial almond-like geometry. Additionally, no acoustic peaks were present in the final spectra.

In the current Big Bang paradigm, the quark-gluon plasma is the state of matter permeating the universe right after inflation. Curiously, the scale of QGP anisotropies is considerably larger ($\ell \leq 20$) than the CMB ones ($\ell > 100$), even though the size of the universe at recombination is much larger than the size of the QGP droplet in LHC and RHIC. While the peaks of the

heavy-ion spectrum tell of initial anisotropies, the CMB peaks are related to the curvature of the universe and matter densities.

ACKNOWLEDGMENTS

I would like to thank Poul Henrik Damgaard for the discussions and incentive on writing this paper. I am also grateful to Christian Bourjau for bringing to the table the possible issue of vertex selection. Finally, I thank Ante Bilandzic, J. J. Gaardhøje, Pavel Naselsky, Hao Liu and You Zhou for the interesting discussions. This work was partly supported by the Danish National Research Foundation (DNRF) and the Conselho Nacional de Desenvolvimento Científico e Tecnológico (CNPq).

-
- [1] K. Aamodt *et al.* (ALICE), Phys. Lett. **B696**, 30 (2011), arXiv:1012.1004 [nucl-ex].
 - [2] S. Chatrchyan *et al.* (CMS), Phys. Rev. Lett. **107**, 052302 (2011), arXiv:1105.4894 [nucl-ex].
 - [3] G. Aad *et al.* (ATLAS), Phys. Rev. Lett. **105**, 252303 (2010), arXiv:1011.6182 [hep-ex].
 - [4] A. A. Penzias and R. W. Wilson, APJ **142**, 419 (1965).
 - [5] Y. Akrami *et al.* (Planck), (2018), arXiv:1807.06205 [astro-ph.CO].
 - [6] S. A. Voloshin, A. M. Poskanzer, and R. Snellings, Landolt-Bornstein **23**, 293 (2010), arXiv:0809.2949 [nucl-ex].
 - [7] U. Heinz and R. Snellings, Ann. Rev. Nucl. Part. Sci. **63**, 123 (2013), arXiv:1301.2826 [nucl-th].
 - [8] H. Song, Y. Zhou, and K. Gajdosova, Nucl. Sci. Tech. **28**, 99 (2017), arXiv:1703.00670 [nucl-th].
 - [9] V. Khachatryan *et al.* (CMS), Phys. Rev. **C92**, 034911 (2015), arXiv:1503.01692 [nucl-ex].
 - [10] M. Aaboud *et al.* (ATLAS), Phys. Rev. **C95**, 064914 (2017), arXiv:1606.08170 [hep-ex].
 - [11] W. Li, *Proceedings, 26th International Conference on Ultra-relativistic Nucleus-Nucleus Collisions (Quark Matter 2017): Chicago, Illinois, USA, February 5-11, 2017*, Nucl. Phys. **A967**, 59 (2017), arXiv:1704.03576 [nucl-ex].
 - [12] G. Denicol, A. Monnai, and B. Schenke, Phys. Rev. Lett. **116**, 212301 (2016), arXiv:1512.01538 [nucl-th].
 - [13] M. Machado, P. H. Damgaard, J. J. Gaardhøje, and C. Bourjau, Phys. Rev. C **99**, 054910 (2019).
 - [14] ALICE Collaboration, “Pb-Pb data sample at 2.76TeV from run number 139465. CERN Open Data Portal.”.
 - [15] C. Bourjau, “mALICE: An open source framework for analyzing alice’s open data,” (2018–).
 - [16] Z.-W. Lin, C. M. Ko, B.-A. Li, B. Zhang, and S. Pal, Phys. Rev. C **72**, 064901 (2005).
 - [17] The ALICE Collaboration, “The ALICE experiment at the CERN LHC,” (2008).
 - [18] B. B. Abelev *et al.* (ALICE), Int. J. Mod. Phys. **A29**, 1430044 (2014), arXiv:1402.4476 [nucl-ex].
 - [19] G. Dellacasa *et al.* (ALICE), (1999).
 - [20] G. Dellacasa *et al.* (ALICE), (2000).
 - [21] P. Cortese *et al.* (ALICE), (2004).
 - [22] K. M. Górski *et al.*, The Astrophysical Journal **622**, 759 (2005).
 - [23] J. Adam *et al.* (ALICE), Phys. Rev. Lett. **116**, 132302 (2016), arXiv:1602.01119 [nucl-ex].
 - [24] A. Bilandzic, R. Snellings, and S. Voloshin, Phys. Rev. C **83**, 044913 (2011).
 - [25] A. Bilandzic, C. H. Christensen, K. Gulbrandsen, A. Hansen, and Y. Zhou, Phys. Rev. **C89**, 064904 (2014), arXiv:1312.3572 [nucl-ex].
 - [26] S. Voloshin and Y. Zhang, Z. Phys. **C70**, 665 (1996), arXiv:hep-ph/9407282 [hep-ph].
 - [27] A. M. Poskanzer and S. A. Voloshin, Phys. Rev. **C58**, 1671 (1998), arXiv:nucl-ex/9805001 [nucl-ex].
 - [28] X.-N. Wang, Phys. Rev. D **43**, 104 (1991).
 - [29] X.-N. Wang and M. Gyulassy, Phys. Rev. D **44**, 3501 (1991).
 - [30] X.-N. Wang and M. Gyulassy, Phys. Rev. D **45**, 844 (1992).
 - [31] M. Gyulassy and X.-N. Wang, Computer Physics Communications **83**, 307 (1994).
 - [32] Z.-w. Lin and C. M. Ko, Phys. Rev. C **65**, 034904 (2002).
 - [33] Z.-w. Lin, C. M. Ko, and S. Pal, Phys. Rev. Lett. **89**, 152301 (2002).
 - [34] Z.-W. Lin and C. M. Ko, Journal of Physics G: Nuclear and Particle Physics **30**, S263 (2003).
 - [35] B. Zhang, Computer Physics Communications **109**, 193 (1998).
 - [36] B.-A. Li and C. M. Ko, Phys. Rev. C **52**, 2037 (1995).
 - [37] B.-A. LI, A. T. SUSTICH, B. ZHANG, and C. M. KO, International Journal of Modern Physics E **10**, 267 (2001), <https://doi.org/10.1142/S02183013010000575>.
 - [38] Z.-W. Lin, Phys. Rev. **C90**, 014904 (2014), arXiv:1403.6321 [nucl-th].
 - [39] W. Broniowski and W. Florkowski, Phys. Rev. C **65**, 024905 (2002).
 - [40] G. Aad *et al.* (ATLAS), Phys. Rev. **C86**, 014907 (2012), arXiv:1203.3087 [hep-ex].
 - [41] J. Silk, Astrophys. J. **151**, 459 (1968).
 - [42] P. Naselsky *et al.*, Phys. Rev. **C86**, 024916 (2012), arXiv:1204.0387 [hep-ph].

- [43] F. J. Llanes-Estrada and J. L. Muoz Martinez, Nucl. Phys. **A970**, 107 (2018), arXiv:1612.05036 [hep-ph].
- [44] G. Sarwar, S. K. Singh, and J.-e. Alam, Int. J. Mod. Phys. **A33**, 1850121 (2018), arXiv:1711.03743 [nucl-th].
- [45] L.-Y. Zhang, J.-H. Chen, Z.-W. Lin, Y.-G. Ma, and S. Zhang, Phys. Rev. C **99**, 054904 (2019).